International Journal of Plasticity 25 (2009) 920–941

Contents lists available at ScienceDirect

International Journal of Plasticity

journal homepage: www.elsevier.com/locate/ijplas

X-ray microdiffraction and strain gradient crystal plasticity studies of geometrically necessary dislocations near a Ni bicrystal grain boundary

Tetsuya Ohashi [a], R.I. Barabash [b,*], J.W.L. Pang [b], G.E. Ice [b], O.M. Barabash [b]

[a] Kitami Institute of Technology, Koencho 165, Kitami 090-8507, Japan
[b] Oak Ridge National Laboratory, Materials Science and Technology, One Bethel Valley Road, Oak Ridge, TN 37831, USA

ARTICLE INFO

Article history:
Received 31 December 2007
Received in final revised form 3 April 2008
Available online 23 May 2008

Keywords:
Crystal plasticity
Dislocations
Grain boundaries
Stress relaxation
Polycrystalline material

ABSTRACT

We compare experimental measurements of inhomogeneous plastic deformation in a Ni bicrystal with crystal plasticity simulations. Polychromatic X-ray microdiffraction, orientation imaging microscopy and scanning electron microscopy, were used to characterize the geometrically necessary dislocation distribution of the bicrystal after uniaxial tensile deformation. Changes in the local crystallographic orientations within the sample reflect its plastic response during the tensile test. Elastic strain in both grains increases near the grain boundary. Finite element simulations were used to understand the influence of initial grain orientation and structural inhomogeneities on the geometrically necessary dislocations arrangement and distribution and to understand the underlying materials physics.

© 2008 Elsevier Ltd. All rights reserved.

1. Introduction

During deformation, dislocations self-organize into complex inhomogeneous substructures that are observed even for initially perfect single crystals (Kocks and Mecking, 2003; Arsenlis and Parks, 1999; Arsenlis et al., 2004; Huang et al., 2000; Gao et al., 1999). Preexisting defects and symmetry breaking boundary conditions increase the subsequent inhomogeneities (Kocks and Mecking, 2003) and dislocation organization becomes more inhomogeneous as deformation proceeds (even when slip is mainly homogeneous). Understanding how dislocations multiply and organize during deformation is important as dislocation substructures affect subsequent materials behavior. Fortunately, emerging

* Corresponding author. Tel.: +1 865 2417230; fax: +1 865 5747659.
E-mail address: barabashr@ornl.gov (R.I. Barabash).

0749-6419/$ - see front matter © 2008 Elsevier Ltd. All rights reserved.
doi:10.1016/j.ijplas.2008.04.009

experimental and theoretical tools promise to provide new insights. For example, strain gradient plasticity models can now predict the influence of different loading conditions on the formation of geometrically necessary dislocations in polycrystalline materials (Bardella, 2007; Bonifaz and Richards, 2008; Beyerlein and Tome, 2008; Gurtin, 2008; Han et al., 2007; Wang et al., 2007; Volokh and Trapper, 2007; Sauzay, 2004; Tschopp and McDowell, 2008), and X-ray microdiffraction can measure the local density of geometrically necessary dislocations, ρ_G, and their density tensor (Larson et al., 2007, 2002; Levine et al., 2006; Ice and Barabash, 2007; Barabash and Ice, 2005).

Grain boundaries and triple junctions are particularly important locations of inhomogeneous deformation because of the conditions for strain compatibility necessary to accommodate the shape and orientation changes in neighbor grains (Huang et al., 2008; Jakobsen et al., 2006; Romanov, 2003; Hansen, 2005; Hansen and Hughes, 1995; Bay et al., 1992). Boundaries may also impede the mobility of dislocations or create additional constraints for the local plastic response of the material. Dislocations can partially penetrate through the incidental dislocation boundaries (IDBs), while they practically cannot penetrate through the geometrically necessary boundaries (GNBs) (Barabash and Pantleon, 2004). In general, boundaries influence the distribution of both geometrically necessary (GN) and Statistically Stored (SS) dislocations.

Recently, strain studies of bicrystal specimens have become popular due to their simple geometry (Spearot et al., 2007, 2005; Monzen et al., 2005; Feng et al., 2003; Chen et al., 2004; Miura et al., 2004, 2003; Ziegler et al., 2003; Lu et al., 2003; Sun et al., 2000). This paper presents an analysis of GN and SS dislocation distributions, and local lattice curvature in a natural Ni bicrystal during *in situ* uniaxial tensile straining. Experimental measurements and model calculations are carried out as a function of depth from the sample free surface and distance from the grain boundary. Two procedures were exploited for the analyses of the mesoscale dislocation density tensor: (1) depth resolved measurements with differential aperture X-ray microscopy (DAXM), which provides detailed point-to-point lattice orientation as a function of depth for each probed location (Larson et al., 2007); (2) streak analyses, which determines the low limit number of GNDs and their density tensor within each probed region (Ice and Barabash, 2007; Barabash and Ice, 2005). The main objective of this paper is to compare the results of experimental and numerical analyses, and to induce some physical insights into the non-uniform deformation near grain boundaries.

2. Method of experiments and numerical simulations

2.1. Ni bicrystal preparation

A Ni bicrystal (>99.9% purity) was prepared by the vertical Bridgman technique. The orientations of the two grains forming the bicrystal were determined by standard Laue X-ray back-reflection. A tensile sample was cut from the bicrystal by electrical discharge machine. The sample surface was then electropolished with an electrolyte of HNO_3 and methanol. The grain boundary was revealed by etching the sample with 1:1 HNO_3 and acetic acid. The sample was cut such that the grain boundary is at the mid-length and almost perpendicular to the tensile axis. The final sample dimensions are

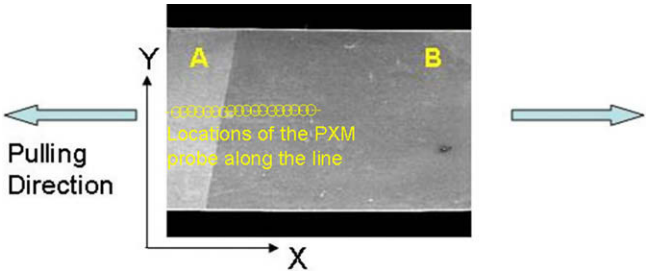

Fig. 1. SEM image of the Ni bicrystal tensile sample after deformation with the schematic of PXM probing locations and the Cartesian reference frame.

$8.43 \times 0.68 \times 0.6\ mm^3$. A laboratory Cartesian reference frame was set such that the loading direction is aligned along the *X*-axis. The orientations of the grains with respect to the tensile axis are shown in Fig. 1. Initial inhomogeneities other than the grain boundary, such as subboundaries or non-uniform distributions of impurities and grown-in dislocations are also supposed to exist in the specimen due to the technique used in the specimen preparation and relatively low purity of the material. Effects of such inhomogeneities are discussed in the Section 3.4.

2.2. 3D polychromatic X-ray microdiffraction

Polychromatic X-ray microdiffraction (PXM) offers a fundamentally new approach to the study of mesoscale dynamics in single and polycrystalline materials (Larson et al., 2007, 2002; Ice and Larson, 2002; Ice and Barabash, 2007; Levine et al., 2006). The PXM technique uses a modified Laue diffraction method based on polychromatic X-ray radiation and allows for 3D mapping of crystalline phase, orientation, elastic strain and plastic deformation with unprecedented spatial resolution. As the polychromatic beam penetrates the sample, it produces a Laue pattern in each subgrain that it intercepts. The overlapping Laue patterns from grains probed by the beam, are recorded by a CCD camera positioned at 90° to the incident beam.

In the DAXM technique the origin of each Laue pattern can be decoded with a wire that scans through the diffracted beams and shadows different portions of the diffracted intensity. These partially shadowed images corresponding to certain locations of the wire, together with the initial depth integrated Laue pattern are used to reconstruct the intensity origin of the overlapping Laue patterns. This decoding technique is called differential aperture X-ray microscopy (DAXM). Lattice rotations as a function of depth, can be resolved by DAXM with a resolution of $\sim$1 μm (Larson et al., 2007, 2002; Levine et al., 2006). The detailed description of experimental characterization of the mesoscale dislocation density tensor with DAXM is described by Larson et al. (2007).

First large area was probed along several lines perpendicular to the boundary (Fig. 1), and the zones of large plastic deformation were determined via streak analysis (Ice and Barabash, 2007; Barabash and Ice, 2005). Then in several specific locations near the boundary the depth resolved DAXM measurements of point-to-point lattice orientations were performed.

In a typical experiment, the sample is mounted on a precision 3-axis rectilinear sample stage. A region of interest is identified using an optical microscope and the (polychromatic) X-ray beam is focused onto the sample. The orientation of each subgrain is (precisely) determined by an automated indexing program (Larson et al., 2007, 2002). Details on the experimental setup and the method of data collection are described elsewhere (Larson et al., 2007, 2002; Ice and Barabash, 2007). PXM experiments were carried out on station 34-IDE at the Advanced Photon Source. The initial lattice orientations and subsequent local rotation in the bicrystal specimen were determined during *in situ* uniaxial tensile deformation at 0%, 12% and 16% macroscopic plastic strain.

The incident X-ray beam was parallel to the *Y*-axis and the sample surface inclined at 45° to the incident beam. Dimensions of the beam were $\sim$0.46 by 0.55 μm^2 with a penetration depth of $\sim$40 μm for the Ni sample.

Scanning electron (SEM) and the orientation imaging microscopy (OIM) images, based on electron backscattering diffraction, were also collected using a Philips XL30 field-emission scanning electron microscope equipped with a DigiView camera.

2.3. Streak analysis of GNDs induced lattice re-orientation

Dislocations displace atoms from their initial positions in the undeformed crystal. Such atomic displacements change the diffraction conditions and broaden the region of high intensity around each Bragg position (Ice and Barabash, 2007; Barabash et al., 2001). Streak analysis is complementary to the DAXM measurements. Below this analysis is expanded for the case of multiple slip.

In the PXM technique, a crystal scatters the white beam into a characteristic Laue pattern that depends on the crystal space lattice, its orientation and the incident-beam energy distribution. The direction of the scattered polychromatic radiation from a deformed grain is characterized by a *unit* vector, $\hat{\mathbf{k}} = \mathbf{k}/\mid \mathbf{k} \mid$. The misorientation between the unit vectors parallel to a Bragg reflection (*hkl*), $\hat{\mathbf{k}}_{hkl}$, and an

arbitrary direction in its vicinity, $\hat{\mathbf{k}}$ near a Bragg reflection is defined (Ice and Barabash, 2007; Barabash and Ice, 2005; Barabash et al., 2001) as a vector, $\mathbf{m} = \hat{\mathbf{k}} - \hat{\mathbf{k}}_{hkl}$. The recorded intensity in PXM is a function of the misorientation vector, m.

For an equal number of random "+**b**" and "−**b**" SS dislocations the broadening of the diffracted intensity is induced by random local fluctuations in the unit cell orientations and the interatomic distance, d, in different locations near a dislocation line that tend to cancel out over (long) length scales. For example, due to the character of the displacement field around edge dislocation, displacements occur only in planes perpendicular to the direction of dislocation line $\boldsymbol{\tau}$. As a result, coherence does not change along the dislocation line direction and the diffracted intensity in this direction is the same as for crystals without dislocations. The size of X-ray spot in our experiment is about ~0.5 μm in diameter with the penetration depth about ~40 μm, and we suppose paired dislocations in this area with 0.5 × 0.5 × 40 μm are detected as SS dislocations.

The unpaired GN dislocation density varies throughout a crystal due to inhomogeneous plastic deformation. The GN portion of dislocation content is due to the incompatibility of plastic deformation and to the local curvature of the corresponding crystal lattice. In other words, GNDs must arise in non-uniformly deformed crystals to maintain the continuity of the crystal lattice. GN dislocations are length scale dependent; at a differential (microscale) volume level, all dislocations are "geometrically necessary" (Arsenlis et al., 2004; Arsenlis and Parks, 1999; Nabarro, 2001; Nye, 1953). Therefore, when we discuss GN portion of dislocation population the representative volume element (RVE) over which the GND's density is determined should be described explicitly (Arsenlis et al., 2004; Arsenlis and Parks, 1999).

The GN portion of dislocation population within each RVE causes lattice curvature (bending and/or twisting). When the X-ray beam probes a region with a curved lattice it intercepts layers with distinct orientations. Differently oriented layers scatter X-rays in different directions. For this reason instead of a sharp intensity maximum (Laue spot) scattering occurs over an angle interval. This "streaking" of the Laue spots changes as the probed region moves through the sample: the change in the GN portion of dislocation content and lattice curvature is accompanied by the change in the PXM intensity distribution. The lattice curvature K (in the first approximation) can be modeled by a network of randomly distributed unpaired GN dislocations with the density ρ_G and Burgers vector **b**. The curvature $K = \rho_G b$ coincides with the effective strain gradient, $\eta = \sqrt{c_1\eta_{iik}\eta_{jjk} + c_2\eta_{ijk}\eta_{ijk} + c_3\eta_{ijk}\eta_{kji}}$ (Huang et al., 2000; Gao et al., 1999), $\eta = K = \rho_G b$. The GN dislocation density tensor $\rho_{G,ik}$ can be re-written in terms of the distortion tensor $\omega_{ij} = u_{j,i}$, and in terms of strain gradient tensor η_{lmk} as follows:

$$\rho_{G,ik} = -\frac{1}{b}\varepsilon_{ilm}\eta_{lmk} = -\frac{\varepsilon_{ilm}}{b}\frac{\partial\omega_{mn}}{\partial x_l}, \quad \text{and} \quad \eta_{lmk} = \partial^2 u_k/\partial x_l \partial x_m; \quad \mathbf{u}_k = \sum_t c_t \mathbf{u}_{kt}. \tag{1}$$

In this equation, ε_{klm} is the permutation symbol, b is the magnitude of the Burgers vector, u_k is the k component of the displacement field **u** for any unit cell from the equilibrium positions $\mathbf{R}_i^0$; c_t is the random number describing the position of dislocation line. The displacement **u** of each unit cell is due to all dislocations in the RVE (Ice and Barabash, 2007; Barabash and Ice, 2005; Barabash et al., 2001).

To find the GN dislocation arrangement in a real crystallographic lattice we need to know the Burgers vector and line direction of the dislocation. Burgers vector usually does not change along the dislocation line. The line direction is free to occupy any direction on the slip plane but we can determine the direction if we have edge and screw components of the dislocation separately.

In plastically strained crystals with GN dislocations the general expression for scattering by crystals with dislocations depends on the pair correlations between displacements of every two scattering cells s and s', $\mathbf{u}_{St} - \mathbf{u}_{S't}$. It is given by a general expression:

$$I(\mathbf{q}) = f^2 \sum_{s,s'} e^{i\mathbf{q}\cdot\Delta R} e^{-T(R_S^0,\Delta R)}, \quad T = c^D \sum_t 1 - e^{(i\mathbf{Q}\cdot(\mathbf{u}_{St} - \mathbf{u}_{S't}))}. \tag{2}$$

Here f is the average scattering factor of the matrix atoms, $\Delta\mathbf{R} = \mathbf{R}_S^0 - \mathbf{R}_{S'}^0 \Delta\mathbf{R} = \mathbf{R}_i^0 - \mathbf{R}_j^0$ is the undistorted distance vector between two scattering cells s and s'; $\mathbf{R}_S^0$ is a position vector of the cell s in the defect-free crystal; c^D indicates the fraction of lattice sites intercepted with dislocations. The diffusely scattered intensity about the centroid of the Laue spot depends on the deviation $\mathbf{q} = \mathbf{Q} - \mathbf{G}_{hkl}$

between the diffraction vector $\mathbf{Q}$ and the momentum transfer $\mathbf{G}_{hkl}$ for an (hkl) Laue reflection. The correlation function T differs according to dislocation arrangement. In general for an arbitrary distribution of paired and unpaired dislocations, the correlation function has both imaginary and real parts $T = T_1 + T_2 + T_3$. The details of the correlation function analysis can be found elsewhere (Ice and Barabash, 2007; Barabash and Ice, 2005). The first term, T_1, is imaginary, linear with respect to the density of unpaired dislocations n^+ and goes to zero when $n^+ = 0$.

$$T_1 = i\sum_{t\alpha} c_\alpha^D(\mathbf{R}_{ss'}\nabla)(\mathbf{G}_{hkl}\mathbf{u}_{st\alpha}); \quad T_2 = -\sum_{\alpha} c_\alpha^D[1-\cos[(\mathbf{R}_{ss'}\nabla)(\mathbf{G}_{hkl}\mathbf{u}_{st\alpha})]];$$

$$T_3 = \frac{i}{2}\sum_{\alpha t} c_\alpha^D \cos[(\mathbf{R}_{ss'}\nabla)(\mathbf{G}_{hkl}\mathbf{u}_{st\alpha})](\mathbf{R}_{ij}\nabla)^2(\mathbf{G}_{hkl}\mathbf{u}_{st\alpha}).$$

Here h, k, l denote the Miller indices of the reflection, $\mathbf{G}_{hkl}$ is a momentum transfer for this reflection, α numerates different slip systems, s and s' are two scattering cells. The real part of the correlation function T_2 is independent of whether dislocations are paired or unpaired. The real part of the correlation function depends only on the total (SS + GN) dislocation density.

For strained crystals with GN dislocations the linear imaginary part T_1 makes the most significant contribution to the correlation function. Part T_3 is also imaginary and typically with $T_3 \ll T_1$ it may be neglected. Since displacements of the lattice sites from their ideal positions decrease very slowly with their distance from dislocations, the main contribution to the T_1 is made by the range of large distances from the dislocation for which we can replace $\sin(Qu_{ss't}) \approx Qu_{ss't}$ and retain only first term of the expansion in powers of distance vector between s and s' cells in the undeformed crystal,

$$\Delta R = \mathbf{R}_s^0 - \mathbf{R}_{s'}^0;$$

$$T_1(\mathbf{R}_S^0, \Delta\mathbf{R}) = -\sum_{\alpha} c_\alpha^D \sum_t \Delta R \frac{\partial}{\partial R_S^0} Qu_{St\alpha} \quad \text{or} \quad T_1(\mathbf{R}_S^0, \Delta\mathbf{R}) = \mathbf{R}_S^0 \mathbf{A}\Delta\mathbf{R}.$$

This term in the correlation function is associated with the *mean bending or torsion* of the crystal lattice within the probed region. It can be expressed in terms of the distortion tensor components $\omega_{ij} = u_{j,i}$ produced by the GN population within probed region (Eq. (1)) Vector $\mathbf{A}$ defines the contrast factors when multiple slip systems with edge and screw dislocations are simultaneously activated within a RVE:

$$\mathbf{A} = \sum_{\alpha} \rho_G bQ(\mathbf{n}_S\mathbf{b}_\alpha)[\tau_\alpha \times \mathbf{g}], \quad \mathbf{n}_s = \frac{\mathbf{R}_S^0}{R_S^0} \quad \text{(edge GNDs)}, \tag{3a}$$

$$\mathbf{A} = \frac{1}{2}\sum_{\alpha} \rho_G bQ\{[\mathbf{n}_S \times \mathbf{g}] - 2(\mathbf{b}_\alpha\mathbf{n}_S)[\mathbf{b}_\alpha \times \mathbf{g}]\} \quad \text{(screw GNDs)}. \tag{3b}$$

It is *important that the vector* $\mathbf{A}$ *is always perpendicular to the direction of diffraction vector* $\mathbf{g} = \mathbf{G}_{hkl}/|\mathbf{G}_{hkl}|$. This is why GNDs (and GNBs) influence the diffraction in the plane transverse to the reciprocal lattice vector (so called orientation space) which is probed with PXM.

The lattice curvature is measured with PXM at each probing location. Two axes ξ and v can be defined along and perpendicular to the streak direction (Ice and Barabash, 2007; Barabash and Ice, 2005) in the plane transverse to the momentum transfer unit vector $\mathbf{g}$. With this coordinate system, the isocontours of the scattered white beam intensity are strongly streaked in the ξ direction, and the full width at half maximum in the ξ direction $FWHM_\xi$ for randomly distributed GN dislocations depends on their density, ρ_G, mutual orientation between the active dislocation system, the momentum transfer unit vector $\mathbf{g}$ (through a contrast factor), and the length of the probed region along GNDs slip direction, L (Ice and Barabash, 2007; Barabash and Ice, 2005; Barabash et al., 2001). In the narrow direction, v, the $FWHM_v$ depends on the average distance between all (GN + SS) dislocations L_s and on the contrast factor for the measured Laue spot C_v. It can be used to estimate the total dislocation density (GN + SS) within each RVE:

$$FWHM_\xi \propto \eta L C_\xi; \quad FWHM_v \propto bL_s^{-1}C_v. \tag{4}$$

Here C_ξ and C_v are contrast factors along and perpendicular to the streak, L is the length of the region probed along the slip direction, and L_s is the average distance between randomly distributed

dislocations. The predominant GNDs density tensor components and direction of the strain gradient can be identified because of their distinctly different contributions to streaking of the Laue patterns.

When straining proceeds the randomly distributed dislocations (both GN and SS) partially collect into walls (Fig. 2). Dislocations of the opposite sign partially annihilate during their grouping within the wall. The GN portion of dislocations within the wall provides a finite rotation between two neighboring mosaic blocks with a rotation angle Θ.

With respect to their origin and properties two main types of dislocation walls/boundaries are distinguished: incidental dislocation boundaries (IDBs) and geometrically necessary boundaries (GNBs) (Kuhlmann-Wilsdorf and Hansen, 1991; Barabash and Pantleon, 2004; Hansen, 2005; Hansen and Hughes, 1995; Hirth et al., 2006). Both types of boundaries are connected with misorientations, which are lower across IDBs than across GNBs (Fig. 2). Thick IDBs result in long-range internal stresses causing the broadening of X-ray reflections both in radial direction of the diffraction vector and in orientation space. GNBs arise from differences in the activated slip systems on both sides of the boundary. Their diffracted intensity distribution becomes highly anisotropic in reciprocal space, which can be used to track the boundary evolution during plastic deformation. For simplicity we describe below the scattering of polychromatic radiation by GNBs (IDBs can be considered similarly).

We define the average distance D between a geometrically necessary boundary (GNBs) and write the number of GNBs per unit length as, $1/D$. This distance corresponds to the second intrinsic length scale of the materials. The total density of GN dislocations grouped in the GNBs is denoted by $\rho_G = 1/Dh$, where h is an average distance between the dislocations within the wall. The effective strain gradient and lattice curvature in this model can be written as, $\eta = K = \Theta/D$. For groupings of GN disloca-

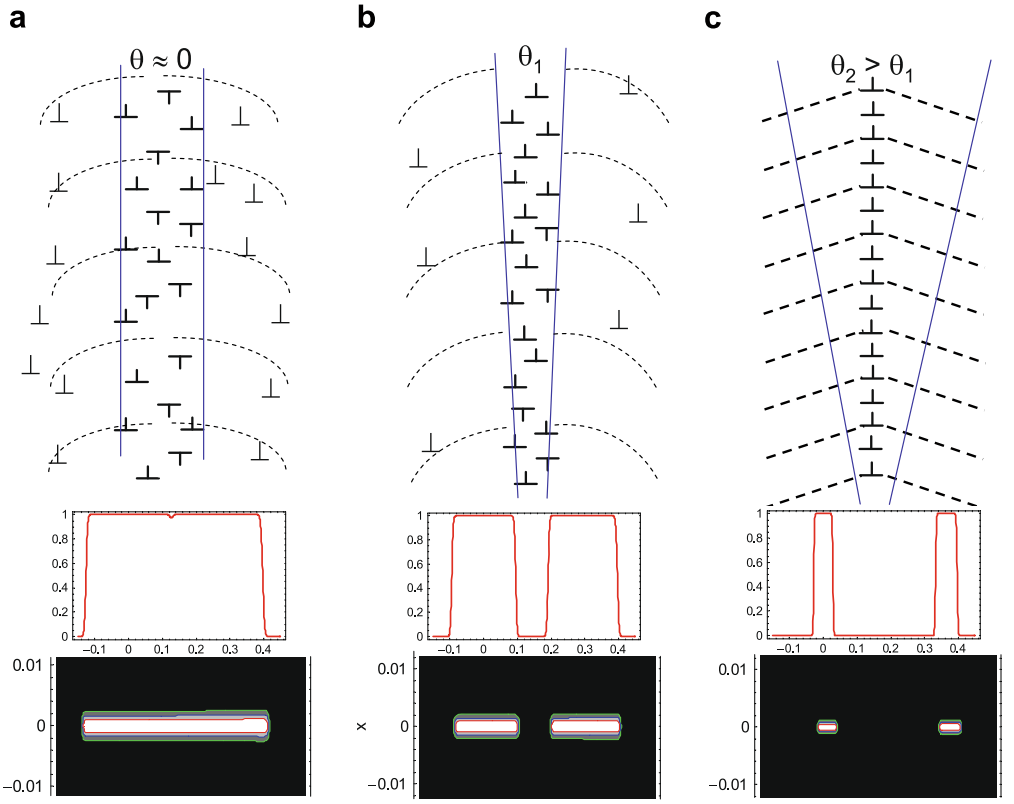

Fig. 2. Sketch of the dislocation grouping within different dislocation walls during straining: (a) thick cell boundary (IDB-1) with almost vanishing disorientation, (b) IDB-2 with significant disorientation and (c) finite rotation through the low angle tilt boundary (GNB). Simulated intensity of the Laue streak profile and 2D image are shown at the bottom of each wall type.

tions within the GN boundaries, GNBs, the $FWHM_{\xi}$ depends on the average distance, D, between GNBs, their mutual orientation to the momentum transfer **G**, the type of GNB (tilt or twist), and the incident X-ray beam direction (Ice and Barabash, 2007; Barabash and Ice, 2005). For crystals with GNDs within the dislocation walls (GNBs or IDBs), X-ray diffraction Laue spots are broadened in proportion to the number of GN dislocations inside the wall and to the total number of walls.

In the case of grouping of some portion of GN dislocations within the boundary and split Laue image (see Fig. 2) the intensity distribution becomes discontinuous due to the finite rotation through the boundary. When the angle through the boundary becomes large enough there will be two separate Laue spots instead of one continuous. The misorientation angle through the boundary can be determined using the centroids of each Laue spots and calculating an average orientation of each region (at least three Laue spots with different (*hkl*) are needed). Misorientation created by the remaining random GN dislocations within each region causes streaking of each Laue spot. In that case total misorientation created by GN dislocations now consists of two parts: (I) infinitesimal misorientation due to GNDs within each region; (II) finite rotation due to GN dislocations grouped within the boundary.

The GN portion of the dislocation population changes the Laue spots intensity distribution much more efficiently than the same amount of SS dislocations. The following criterion (Ice and Barabash, 2007; Barabash and Ice, 2005) can be used to characterize the influence of the GN dislocations on the Laue pattern:

$$\rho_G L > 0.1\sqrt{\rho_{G+S}}. \tag{5}$$

When this condition is satisfied, the GN dislocations cause essential streaking of the Laue pattern. Here L is the size of the RVE, ρ_{G+S} is total density of GN and SS dislocations. For example, if $L = 10\ \mu\text{m}$, $\rho_{G+S} = 10^{12}\ \text{cm}^{-2}$, $\rho_G = 10^9\ \text{cm}^{-2}$. This means that when the GN portion of dislocation population $\rho_G = 0.01\rho_{G+S}$, the Laue image starts to streak. This is in line with the approach of Arsenlis et al. (2004), showing that small amounts of GN dislocations (0.01 and less) may cause essential lattice curvature. More details of the streak analysis of PXM images from deformed crystals can be found elsewhere (Ice and Barabash, 2007; Barabash and Ice, 2005).

2.4. Dislocation model-based strain gradient crystal plasticity analysis

Here we describe our crystal plasticity model. Assumption of infinitesimal deformation is used for simplicity. The maximum nominal tensile strain is 10% and the error due to this assumption is moderate and will be tolerated. Slip deformation is assumed to take place on {1 1 1} crystal planes and in ⟨1 1 0⟩ crystal directions. The activation condition of the slip system n is given by the Schmidt law:

$$P_{ij}^{(n)}\sigma_{ij} = \theta^{(n)}, \quad P_{ij}^{(n)}\dot{\sigma}_{ij} = \dot{\theta}^{(n)} \quad (n = 1, \ldots, 12) \tag{6}$$

and,

$$P_{ij}^{(n)} = \frac{1}{2}(v_i^{(n)}b_j^{(n)} + v_j^{(n)}b_i^{(n)}), \tag{7}$$

where σ_{ij} and $\theta^{(n)}$ denote the stress and the critical resolved shear stress on the slip system n, respectively. The slip plane normal $v_i^{(n)}$ and the slip direction $b_i^{(n)}$ define the Schmid tensor $P_{ij}^{(n)}$. Quantities with dot indicate increments of them. Increment of the critical resolved shear stress is written as follows:

$$\dot{\theta}^{(n)} = \sum_m h^{(nm)}\dot{\gamma}^{(m)}. \tag{8}$$

Here, $\dot{\gamma}^{(m)}$ denotes the increment of plastic shear strain on slip system m. By assuming the infinitesimal strain approximation, the constitutive equation is written as follows (Hill, 1966):

$$\dot{\sigma}_{ij} = \left[S_{ijkl}^{e} + \sum_n \sum_m \{h^{(nm)}\}^{-1} P_{ij}^{(n)} P_{kl}^{(m)}\right]^{-1} \dot{\varepsilon}_{kl}, \tag{9}$$

where S_{ijkl}^{e} denotes elastic compliance. Summation is made over the active slip systems.

The critical resolved shear stress is given by the following equation (Ohashi, 1987, 1994):

$$\theta^{(n)} = \theta_0 + \sum_m \Omega^{(nm)} a\mu\tilde{b}\sqrt{\rho_S^{(m)}}, \tag{10}$$

where θ_0 denotes the lattice friction term and $\rho_S^{(m)}$ denotes the density of statistically stored (SS) dislocations that accumulate on the slip system m. Reaction between dislocations on slip systems n and m defines the magnitude of the interaction matrix $\Omega^{(nm)}$. Diagonal terms in $\Omega^{(nm)}$ are unity and in the present study, we choose off diagonal terms to express pseudo-isotropic hardening character for every slip system. μ and $\tilde{b}$ denote the elastic shear modulus and magnitude of Burgers' vector, respectively. a is a numerical factor, which is equal to 0.1 in this paper.

Increment of the SS dislocations is given as follows:

$$\dot{\rho}_S^{(n)} = c\dot{\gamma}^{(n)}/\tilde{b}L^{(n)}, \tag{11}$$

where c is a numerical coefficient of the order of 1. $L^{(n)}$ denotes the mean free path of dislocations on slip system n and, in this paper, we use the following model for it:

$$L^{(n)} = c^* \Big/ \sqrt{\sum\nolimits_m w^{nm}(\rho_s^{(m)} + \|\rho_G^{(m)}\|)}, \tag{12}$$

where c^* is a material constant of the order of 10–100 (for detailed discussion, see Kuhlmann-Wilsdorf, 1989), and w^{nm} determines the intensity of obstacle effect of dislocations on slip system m to the movement of dislocations on slip system n. We assume that dislocations accumulated on the same slip plane as that of moving dislocations do not contribute to the mean free path ($w^{nm} = 0$), and all the other dislocations contribute equally ($w^{nm} = 1$).

The edge and screw components of the geometrically necessary (GN) dislocations are obtained from the gradients of plastic shear strain on slip systems (Ohashi, 1997)

$$\rho_{g,\text{edge}}^{(n)} = -\frac{1}{\tilde{b}}\frac{\partial\gamma^{(n)}}{\partial\xi^{(n)}}, \quad \rho_{g,\text{screw}}^{(n)} = -\frac{1}{\tilde{b}}\frac{\partial\gamma^{(n)}}{\partial\zeta^{(n)}}. \tag{13}$$

Here, $\xi^{(n)}$ and $\zeta^{(n)}$denote the crystal coordinates of slip system (n), respectively. The norm of two components defines the scalar density for the GN dislocations

$$\|\rho_G^{(n)}\| = \sqrt{(\rho_{G,\text{edge}}^{(n)})^2 + (\rho_{G,\text{screw}}^{(n)})^2}. \tag{14}$$

Evaluation of the edge and screw components for the GN dislocations enables one to calculate the tangent vector $\mathbf{l}^{(n)}$ of the dislocation line segments (Ohashi, 1999)

$$\mathbf{l}^{(n)} = \frac{1}{\|\rho_G^{(n)}\|}(\rho_{G,\text{screw}}^{(n)}\mathbf{b}^{(n)} + \rho_{G,\text{edge}}^{(n)}\mathbf{b}^{(n)} \times \mathbf{v}^{(n)}), \tag{15}$$

and the characteristic angle φ of the dislocation segment

$$\cos\varphi^{(n)} = \frac{\rho_{G,\text{screw}}^{(n)}}{\|\rho_G^{(n)}\|}, \quad \sin\varphi^{(n)} = \frac{\rho_{G,\text{edge}}^{(n)}}{\|\rho_G^{(n)}\|}. \tag{16}$$

Positive and negative edge dislocation segments have the characteristic angles $\pi/2$ and $3\pi/2$, respectively, while positive and negative screw segments have the characteristic angles 0 and π. We can visualize the distribution of the GN dislocation segments with Eqs. (15) and (16) (Ohashi, 2005; Ohashi et al., 2007).

The strain hardening coefficient in Eq. (8) is given by the following equation:

$$h^{(nm)} = \frac{1}{2}ac\mu\Omega^{(nm)} \Big/ \left[L^{(m)}\sqrt{\rho_S^{(m)}}\right], \tag{17}$$

and by substituting Eq. (12) into Eq. (17), we have

$$h^{(nm)} = \frac{ac\mu}{2c^*}\Omega^{(nm)}\sqrt{\frac{\sum_k w^{mk}(\rho_S^{(k)} + \|\rho_G^{(k)}\|)}{\rho_S^{(m)}}}. \tag{18}$$

2.5. Data used for the numerical analysis

Fig. 3 shows the Ni bicrystal specimen and finite element meshing employed for the numerical analysis. The dimension of the specimen is $8.43 \times 0.68 \times 0.6$ mm, equal to that used in the experiment. The specimen is divided into $90 \times 8 \times 4$ elements in x, y and z direction, respectively, and the element type used is the composite type brick element with eight nodes. The specimen is meshed in non-uniform manner in x and y direction which will enable one to follow a possible sharp change of physical quantities in the vicinity of the grain boundary and specimen surface.

We use experimental data for the magnitude of the Burgers' vector ($\tilde{b} = 2.556$ Å) and the elastic compliances (s_{11} = 0.8347, s_{12} = −0.3281, and s_{44} = 0.9804×10^{-11} m^2/N). The elastic anisotropy ratio is 2.372. Therefore, non-uniform deformation takes place near the grain boundary even if the deformation is purely elastic. The initial dislocation density on each slip system is 10^9 m^{-2} and we assume c^* = 10 and θ_0 = 30 MPa.

Crystal orientation is defined by three Euler angles κ, θ and ϕ, definition of which is shown in Fig. 4 and the relation between the crystal- and the specimen-coordinate systems is given by the following equation:

$$\begin{pmatrix} u_{100} \\ u_{010} \\ u_{001} \end{pmatrix} = \begin{pmatrix} \cos\theta & \sin\theta\sin\phi & -\sin\theta\cos\phi \\ \sin k\sin\theta & -\sin k\cos\theta\sin\phi + \cos k\cos\phi & \sin k\cos\theta\cos\phi + \cos k\sin\phi \\ \cos k\sin\theta & -\cos k\cos\theta\sin\phi - \sin k\cos\phi & \cos k\cos\theta\cos\phi - \sin k\sin\phi \end{pmatrix} \begin{pmatrix} x \\ y \\ z \end{pmatrix}. \tag{19}$$

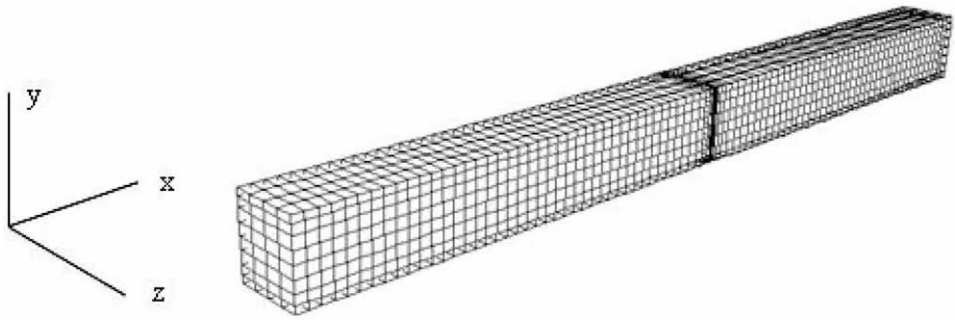

Fig. 3. Ni bicrystal specimen employed for the numerical analysis and its finite element meshing.

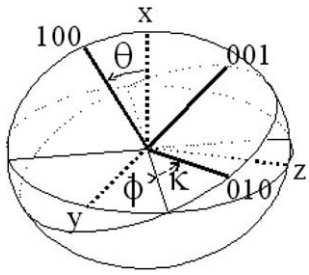

Fig. 4. Definition of Eulerian angles k, θ and ϕ.

In the experiment, the coordinate transformation matrix (orientation matrix) is given numerically (see Section 3). Because the experimental data of the orientation matrix consists of nine numerical values and only three Euler angles are independent, the determination of the Euler angles from the orientation matrix is not straight forward. Therefore, we employed the following procedure: First, we normalize the experimental data of the rotational matrix and then, we solve the nine simultaneous equations by equating each experimental datum for component of rotational matrix with the component given in Eq. (19). Variables to be solved are Euler angles and we obtain two sets of solutions since the simultaneous equations are multiple valued. Lastly, we apply the two sets of Euler angles to Eq. (19) and compare the rotation matrix with experimental data to select one set of Euler angles. The results are summarized in Table 1 which shows good agreement with the experimentally obtained matrices.

Definition of the 12 slip systems of $\{1\,1\,1\}\langle 1\,1\,0\rangle$ are shown in Table 2. When uniaxial tensile load is applied in the X direction and the crystal orientations for two crystal grains are given by those shown in Table 1, the largest Schmid factor in the grain A is 0.4684 which is for the slip system #6, and the second largest value is 0.4338 for the slip system #12. In the grain B, the largest Schmid factor is 0.4909 for the slip system #3 and the second largest value is 0.4333 on slip system #6.

Finite element nodes on the left surface ($x = 0$) of the model are not allowed to move in x direction and the nodes on the right surface ($x = 8.43$ mm) are given a uniform tensile displacement. We gradually increase the tensile displacement on the right surface and monitor the resolved shear stress on 12 slip systems in each finite element. When the resolved shear stress on a slip system reaches its critical value, which is given by Eq. (10), we pause the simulation and revise the strain hardening coefficient for the element. With the new value for the element stiffness, we resume the simulation until the resolved shear stress on a slip system in some element reaches its critical value. We repeat this process of incremental analysis until the macroscopic tensile strain reaches 10%.

Table 1
Euler angles and orientation matrix used for the numerical analysis

Grain	Euler angles (deg)			Orientation matrix		
	κ	θ	ϕ			
A	−83.26	37.48	131.4	0.7936	0.45632	0.40247
				−0.60424	0.51347	0.60930
				0.07138	−0.72672	0.68321
B	22.85	100.6	94.8	−0.18452	0.97937	0.08232
				0.38168	−0.00578	0.92428
				0.90569	0.20197	−0.37274

Table 2
Twelve slip systems defined for face centered cubic crystals

Slip system No.	Schmid–Boas notation	Slip plane	Slip direction	Generic name
1	A2	$1\,1\,1$	$1\,\bar{1}\,0$	Critical slip system
2	A6	↑	$0\,1\,\bar{1}$	↑
3	A3	↑	$1\,0\,\bar{1}$	↑
4	D1	$\bar{1}\,1\,1$	$1\,1\,0$	Cross slip system
5	D6	↑	$0\,1\,\bar{1}$	↑
6	D4	↑	$1\,0\,1$	↑
7	B2	$1\,1\,\bar{1}$	$1\,\bar{1}\,0$	Co-planar slip system
8	B5	↑	$0\,1\,1$	↑
9	B4	↑	$1\,0\,1$	Primary slip system
10	C1	$1\,\bar{1}\,1$	$1\,1\,0$	Conjugate slip system
11	C5	↑	$0\,1\,1$	↑
12	C3	↑	$1\,0\,\bar{1}$	↑

3. Results and discussion

The PXM technique was applied to the complicated dislocation structure arising from the *in situ* uniaxial tensile deformation in a Ni bicrystal (Fig. 1). Diffraction patterns were collected from different sample locations in grains A (left) and B (right) (Fig. 1) by translating the sample under the white microbeam. PXM patterns were recorded along several lines parallel to the sample *x*-axis with a step size of 2 μm. Total 9000 locations were probed. The locations along one of such lines are shown schematically at the SEM image of the sample after deformation (Fig. 1). Although before the deformation the boundary was practically perpendicular to the sample axes, as a result of deformation the boundary became distorted and inclined to the sample axes (this observation will be further discussed in Section 3.3). Moreover the stress state is *not* really uniaxial from the beginning of the deformation because of elastic anisotropy of the material. Not only tensile but also other components of stress are acting on the grain boundary plane. The orientation of undeformed grains was

$$U_A = \begin{bmatrix} 0.7936 & 0.4563 & 0.4025 \\ -0.6051 & 0.5142 & 0.6101 \\ 0.0715 & -0.7277 & 0.6841 \end{bmatrix}, \tag{20a}$$

$$U_B = \begin{bmatrix} -0.1845 & 0.9794 & 0.0823 \\ 0.3743 & -0.0057 & 0.9065 \\ 0.8882 & 0.1981 & -0.3655 \end{bmatrix}. \tag{20b}$$

In grain A the orientation of the surface normal before deformation was almost parallel to $[2\,3\,3]$ with loading direction approximately in the $[1\,\bar{1}\,0]$ direction. In grain B the *x*-axis is close to the $[\bar{1}\,2\,5]$ direction with surface normal close to $[0\,3\,\bar{1}]$ direction. The microbeam-Laue diffraction reveals pronounced streaking of Laue images after 12% and 16% strain. Typical Laue patterns from the deformed A and B grains and the boundary region are shown in Fig. 5. It was possible to track the grain orientation as the step size between neighboring probing locations was 2 μm. The average orientation was well preserved within each grain and it was distinct from the other grain (Fig. 5a and c). Laue beam penetrates approximately 40 μm into the depth of the sample. In the boundary region the overlapping of the two Laue patterns corresponding to both A and B grains was observed. The width of the boundary region was determined as the region where overlapping of Laue patterns from A and B grains were observed. The thickness of boundary region was equal of several micrometers. During the experiment we followed three main phenomena: lattice rotations and elastic and plastic deformation. Plastic response to the uniaxial straining is quite different in the two grains (Fig. 6). In the A grain, zones with intensive plastic deformations are observed in the region of 100 μm close to the boundary, while in the B grain the zones with high plastic activity are concentrated in shear bands and separated with zones with low dislocation density. In both grains plastic deformation is inhomogeneous. Oscillations of GN dislocations are observed even within the shear band. Severe plastic deformation changes the shape of the Laue spot. They become streaked (elongated) in certain direction as described in Section 2.3 and the streaking depends on the predominant GN slip systems operating within the probed region (according to Eq. (4)). Due to inhomogeneous plastic deformation in the grain A the streak length and direction of all Laue spots oscillates strongly over the grain (Fig. 7).

3D measurement of the depth-dependent local lattice orientation were performed with DAXM technique at several specific locations in both grains close to the grain boundary (Fig. 8). It is visible that in both grains the misorientation between the surface and the bulk of the grain increased with the depth. The scale of the depth-dependent misorientation increased when probing location approached the boundary in both grains. In the grain A with higher plastic deformation the depth-dependent misorientation was almost twice higher than at the same distance from the grain boundary in the grain B (compare solid curves in Fig. 8a and b).

3.1. Analysis of the dilatational strain in the vicinity of the boundary

After tensile test both elastic and plastic strain are present in the sample. To analyze possible dilatational elastic strain measurements with a monochromatic microbeam were performed in the two

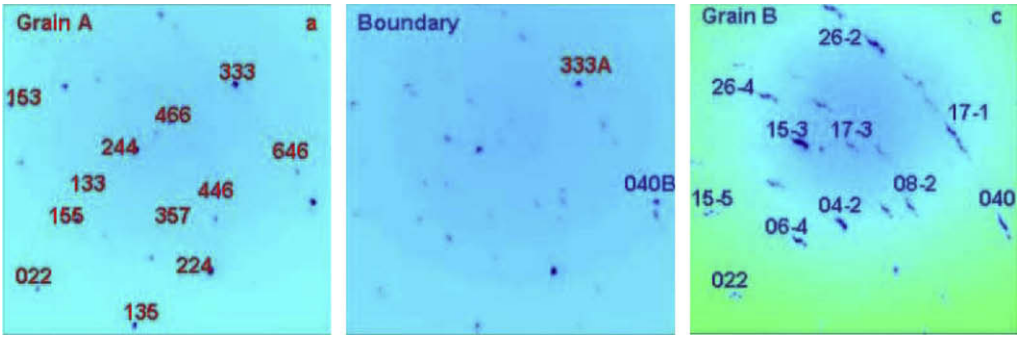

Fig. 5. Typical Laue patterns for grain A (a) the boundary (b) and grain B (c).

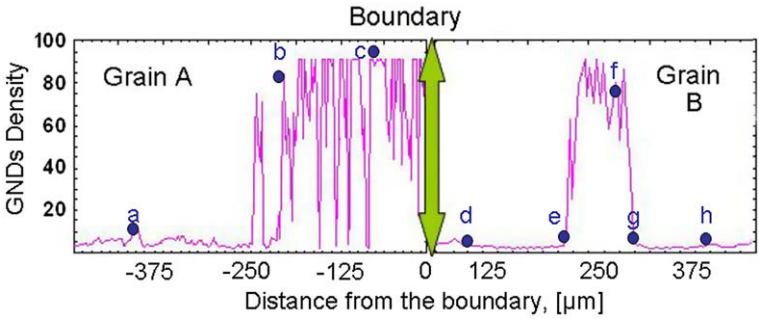

Fig. 6. PXM results for GNDs density oscillations in the vicinity of the boundary between two grains. GNDs density is shown as their % of the maximal value of $1.5 \times 10^{12}\ m^{-2}$.

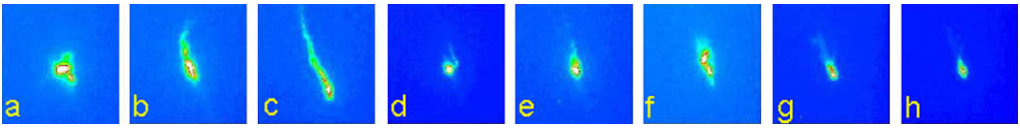

Fig. 7. Example of streak oscillations for (040) Laue spot at different probing locations which are shown by dark circles and labels in Fig. 6.

grains in the vicinity of the boundary. Reflection (224) with $d_{224} = 0.0723$ nm in the unstrained sample was chosen for both neighboring grains (as this Laue spot was observed in both of them). The reciprocal space in the vicinity of the (224) reflection was scanned within the energy interval of 13.871–14.09 keV with a step of 1 eV along the line perpendicular to the boundary (Fig. 9). With the increase of energy of the beam the radius of the Evald sphere changes and at certain energy value the Evald sphere intercepts (224) reciprocal lattice (r.l.) point. Due to orientation and elastic strain change the position of the energy corresponding to the (224) reciprocal lattice point changes for different locations in the grain (Fig. 9a). In the grain A energy increases mainly due to orientation change when the probing location approaches the boundary and remains practically same in the boundary region and at relatively large distance from the boundary in the grain B. In this region of the grain B with highly strained lattice no GN dislocations are observed. Dilatational strain slightly changes with the distance from the boundary in the grains A and B (Fig. 9b). In Fig. 6, where GND density is plotted against position, the higher density in grain A spreads over the width of 250 μm close to the boundary. In the grain B the localized band with strong rotational modes and high density of GN dislocations is

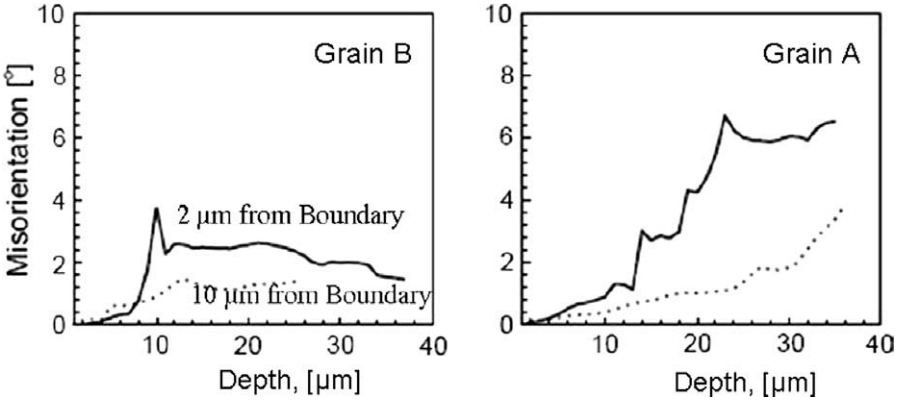

Fig. 8. Change of misorientation with depth at four different positions located at 2 μm (solid line) and 10μm (dashed lines) into the grain B (left) and grain A (right).

relatively narrow with a width of 62.5 μm. It is observed at the distance of ~125 μm away from the boundary (Fig. 6). In the grain A fast oscillations of the GN dislocations take place relatively close to the boundary and only in the vicinity of the boundary the lattice remains strained without visible GN dislocation (Figs. 6 and 9). Such different dislocation substructure in the A and B grains separated by the boundary is in agreement with classification of the near grain boundary structures described by (Hansen, 2005). Typically grain boundaries in the polycrystalline materials are not penetrable for slip dislocations (Hansen, 2005). As a result of interaction between slip dislocations and grain boundaries, different slip band arrangements may form on both sides of the boundaries which is observed in this study. In the grain B slip band is observed in the grain interior but no bands at the boundary. In the grain A slip bands are located much closer to the boundary (Fig. 6). These observations were further supported by SEM/OIM analysis.

3.2. SEM and OIM characterization of the deformed bicrystal

Typical SEM images of the tensile Ni bicrystal are shown in Fig. 10. The distinct plastic response of the two grains is demonstrated in Figs. 10a and b. Bending of slip bands parallel to the boundary is observed in the grain A at the distance of several micrometers from the boundary (Fig. 10a). In the grain B the bands are not observed within a large distance from the boundary. Essentially inhomogeneous plastic deformation in the grain A results in a peculiar shape of a slip band. Some of them demonstrate clear local rotations of the lattice with alternating slip systems in the grain A (Fig. 10d). Many

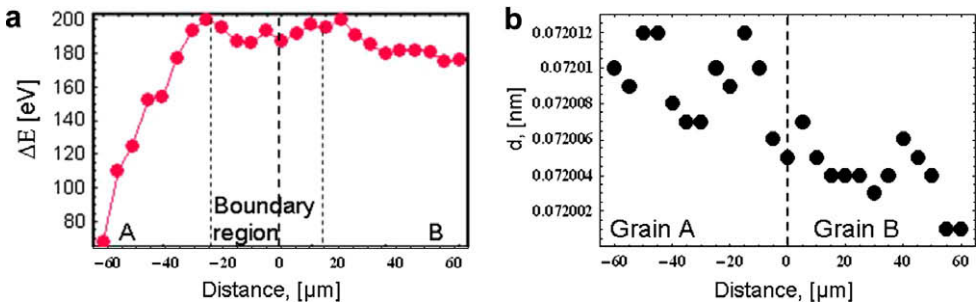

Fig. 9. Change of the energy corresponding to the (2 2 4) reflections (a) and (224) lattice spacing change (b) in the vicinity of the boundary between grains A and B.

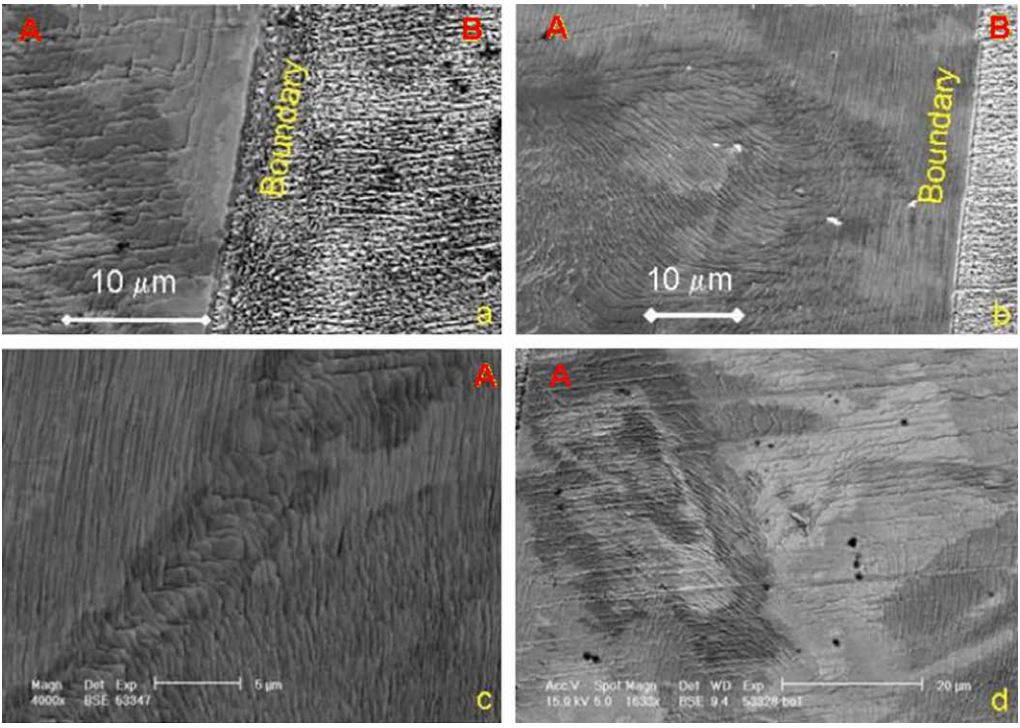

Fig. 10. SEM images of the Ni bicrystal specimen surface: (a,b), slip lines observed near the boundary, (c) typical slip band in the interior of the grain A, and (d) slip localization observed in the interior of the grain A.

narrow (with the size of several microns) relatively straight slip bands were observed in the grain B (Fig. 10c).

The results of OIM analysis of the region in the grain A of the Ni bicrystal are shown in Fig. 11. The chosen area (Fig. 11a) contained a region with a distinct slip band. OIM image was taken with a step size 0.7 μm (Fig. 11b). In this study the orientation obtained by OIM analysis coincided with an average orientation obtained from PXM Laue data. However, OIM analysis is not as sensitive as PXM to small local misorientations and cannot provide information on the depth-dependent misorientations caused by geometrically necessary dislocations (GNDs).

3.3. Numerical results for distribution of plastic shear strain and GN and SS dislocations on slip systems

Fig. 12 shows the experimental (red) and numerically calculated (blue curve) flow curves. The nominal stress versus nominal strain relation obtained by the numerical analysis is very similar to the experimental one. The specimen shows macroscopic yielding when the nominal stress is about 65 MPa and a moderate strain hardening after that. This stress–strain curve shows slight discrepancies with the experimental one. One reason for this discrepancy will be that the numerical analysis assumes that crystal orientation, initial dislocation density, or chemical components etc. are perfectly uniform in each grain. This will not be true for the real material. When there are inhomogeneities, secondary slip systems tend to be activated after some amount of slip on the primary one. Shear strains on secondary systems are usually very small but dislocations on the secondary slip systems work as strong obstacles to moving dislocations on the primary system. This results in a high strain hardening. This kind of slip behavior is widely observed in tensile deformation of single crystals (that is, formation of kink bands and band of secondary slip), and it is believed that this causes the transition from the deformation stage I to II in the deformation curve of single crystals. Fig. 10 shows slip patterns

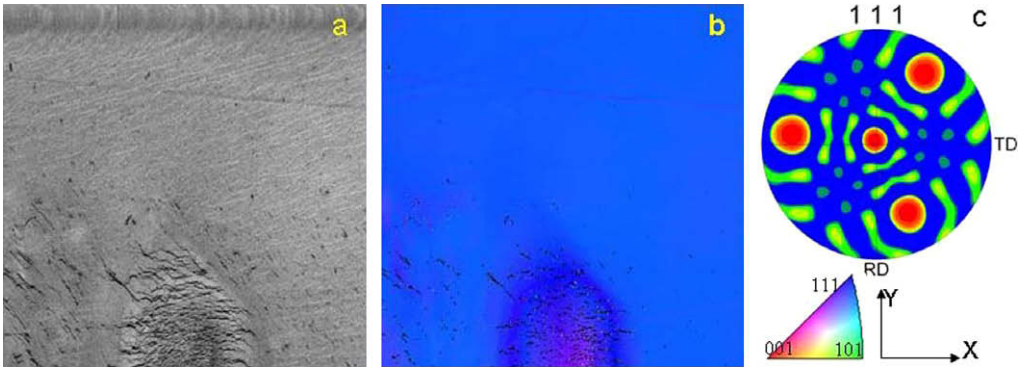

Fig. 11. (a) SEM image of the area in the interior of the grain A; (b) OIM image of this area (orientation map); (c) the pole figure of this region obtained from OIM analysis.

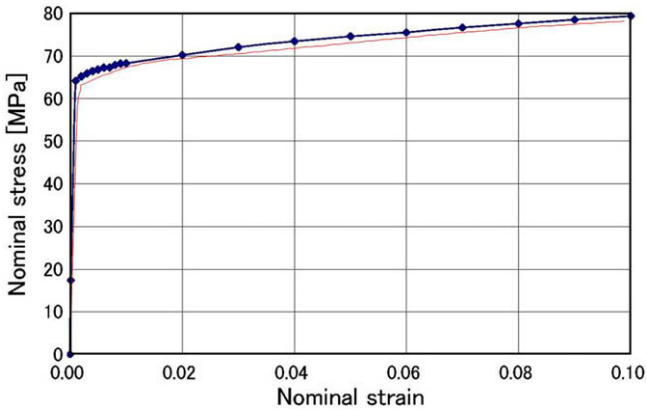

Fig. 12. Numerical (blue curve) and experimental (red curve) results of the load-elongation curve of the Ni bicrystal under tensile deformation.

experimentally observed in the present study when the nominal tensile strain is 12%. Activation of secondary slip systems is observed.

Figs. 13a–d show non-uniform distribution of strain components ε_{xx}, ε_{yy}, ε_{zz}, and ε_{yz} when the nominal strain is 10%. Deformed shape of the specimen is also depicted in Fig. 13a. The specimen looks to be slightly bent and twisted, which is attributed to anisotropic deformation due to plastic slip on slip systems. Such bending and twisting of the sample was observed experimentally. Strain components ε_{xy} and ε_{zx} are not equal to zero, but they are smaller than 5% and are not shown.

Normal component of the strain in tensile direction ε_{xx} is approximately 8% and 14% in the grain A and B, respectively, and it gradually decreases to the value less than 2% in the vicinity of the grain boundary (Fig. 13a). Similar trend is observed in the distribution of ε_{yy} and ε_{zz} (Fig. 13b and c). For example, ε_{yy} is approximately −1% and −10% in the grain A and B, respectively and it decreases nearly equal to zero at the grain boundary. The shear strain component ε_{yz} is approximately 8% in the grain A and −12% in the grain B. This means that grains A and B are sheared in the opposite direction and this causes the twisted shape after deformation.

Figs. 14a–d show the slip activity and accumulation of dislocations on the $(1\,1\,1)[1\,0\,\bar{1}]$ slip system. In the grain A, there is no activity of this slip system, while the plastic shear strain in the interior of the grain B is about −28% and it is suppressed almost completely at the grain boundary. Figs. 14b–c show

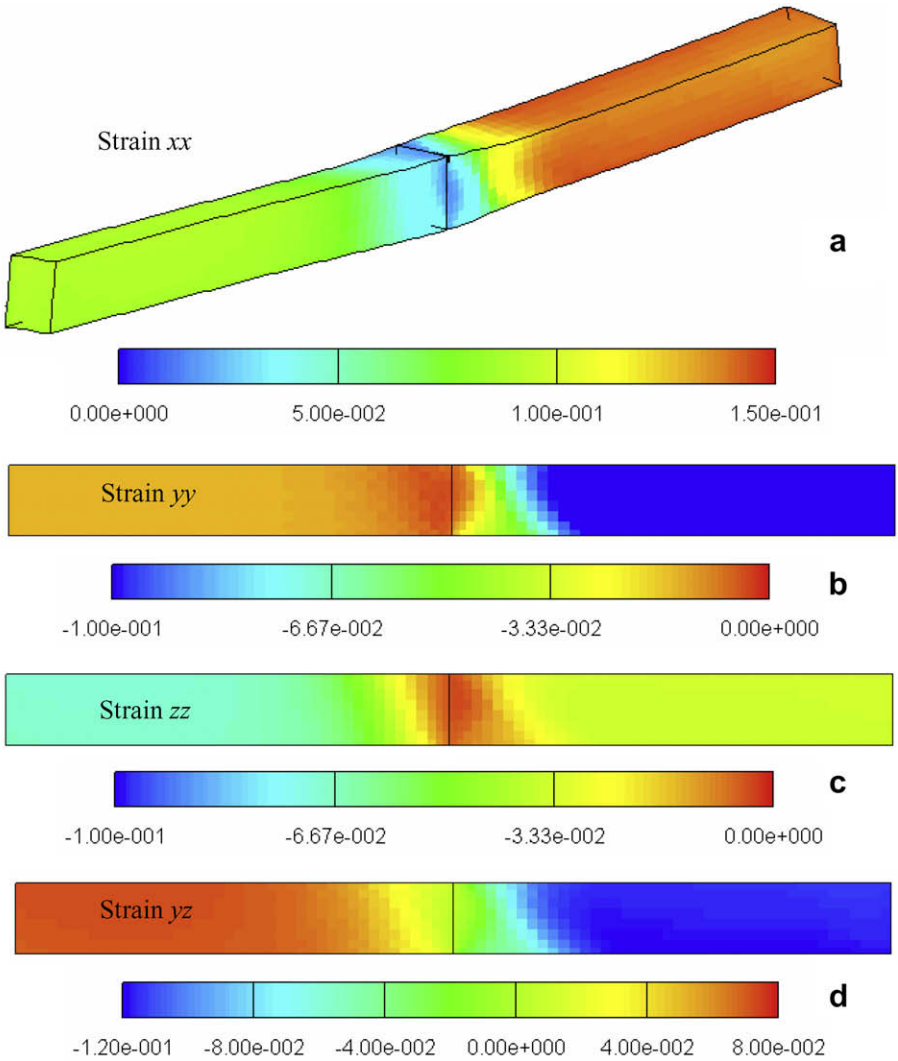

Fig. 13. Analysis results for the deformation of the specimen when the nominal strain is 10%. (a) Distribution of the normal strain ε_{XX} which is mapped on the deformed shape of the bicrystal specimen. Deformation is exaggerated by the factor of 2, (b)–(d) distribution of ε_{YY}, ε_{ZZ} and ε_{YZ} on the cross section at $Z = 0.3$ mm, respectively.

the density distribution of the GN dislocations. A high density band of GN dislocations is formed from the intersection of the grain boundary and the bottom surface of the specimen and grows in the direction approximately 45 degree from the grain boundary (Fig. 14b). The band consists mainly of the edge type dislocations (Fig. 14c) but the dislocations in the vicinity of the grain boundary have mixed type character (Fig. 14c). The bicrystal specimen tends to bend and twist under application of uniaxial tensile load due to the anisotropic nature of slip deformation of two component crystals, which we observed already in Fig. 13a. The anisotropic nature of the deformation of the specimen and the condition of external loading contribute to the formation of high density band of GNDs, although we will not go into details of the mechanism of the formation of the high density band of GNDs.

Fig. 14d shows density distribution of SSDs. The density of SSDs is almost uniform in the region distant from the grain boundary. This result corresponds to the fact that the plastic shear strain on this

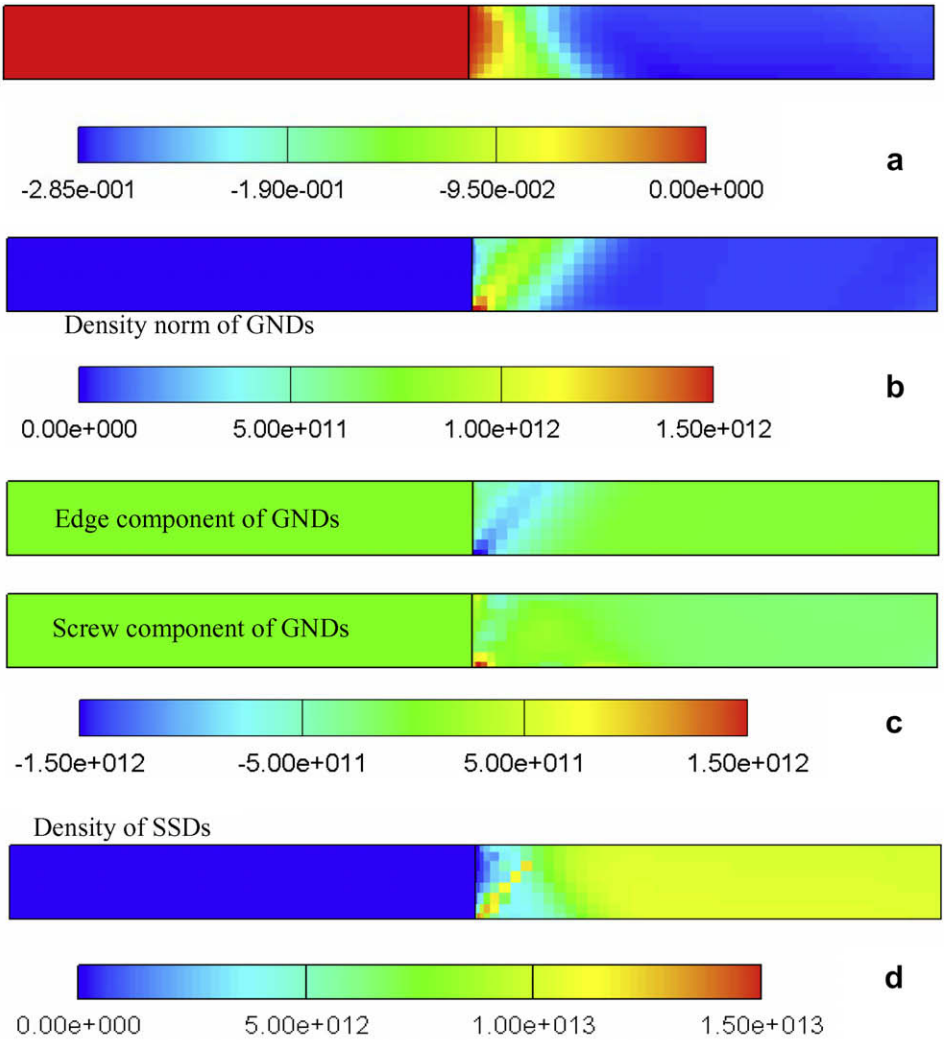

Fig. 14. Distribution of plastic shear strain, density norm of GNDs, edge and screw component of GNDs and SSDs on the $(111)[10\bar{1}]$ slip system when the nominal strain is 10% and viewed on the $Z = 0.3$ mm cross section.

slip system is almost uniform inside the grain and far from the grain boundary. Near the grain boundary, the SSD density gradually decreases, which is also consistent with the result shown in Fig. 14a, and it is worthwhile to note that density of SSDs is also high along the high density band of GNDs. This pattern of SSDs is supposed to have formed after some interaction of GNDs and SSDs. Let us consider this point in detail. The accumulation of SSDs is evaluated by the magnitude of slip strain and dislocation mean free path (Eq. (11)), while the magnitude of slip strain (Fig. 14a) does not show stripe pattern near the grain boundary. Therefore, the high density band of GNDs is supposed to have contributed to the accumulation of SSDs in the stripe pattern. GNDs in the band obstruct movement of dislocations as forest dislocations: the mean free path of moving dislocations on slip systems which have intersecting slip plane with that of the present ($(1\,1\,1)[1\,0\,\bar{1}]$) slip system are shortened (Eq. (12)). Fig. 15d shows the density distribution of SSDs on $(\bar{1}\,1\,1)[1\,1\,0]$ slip system where we also notice a stripe pattern growing from the intersection of the grain boundary and the bottom surface of the

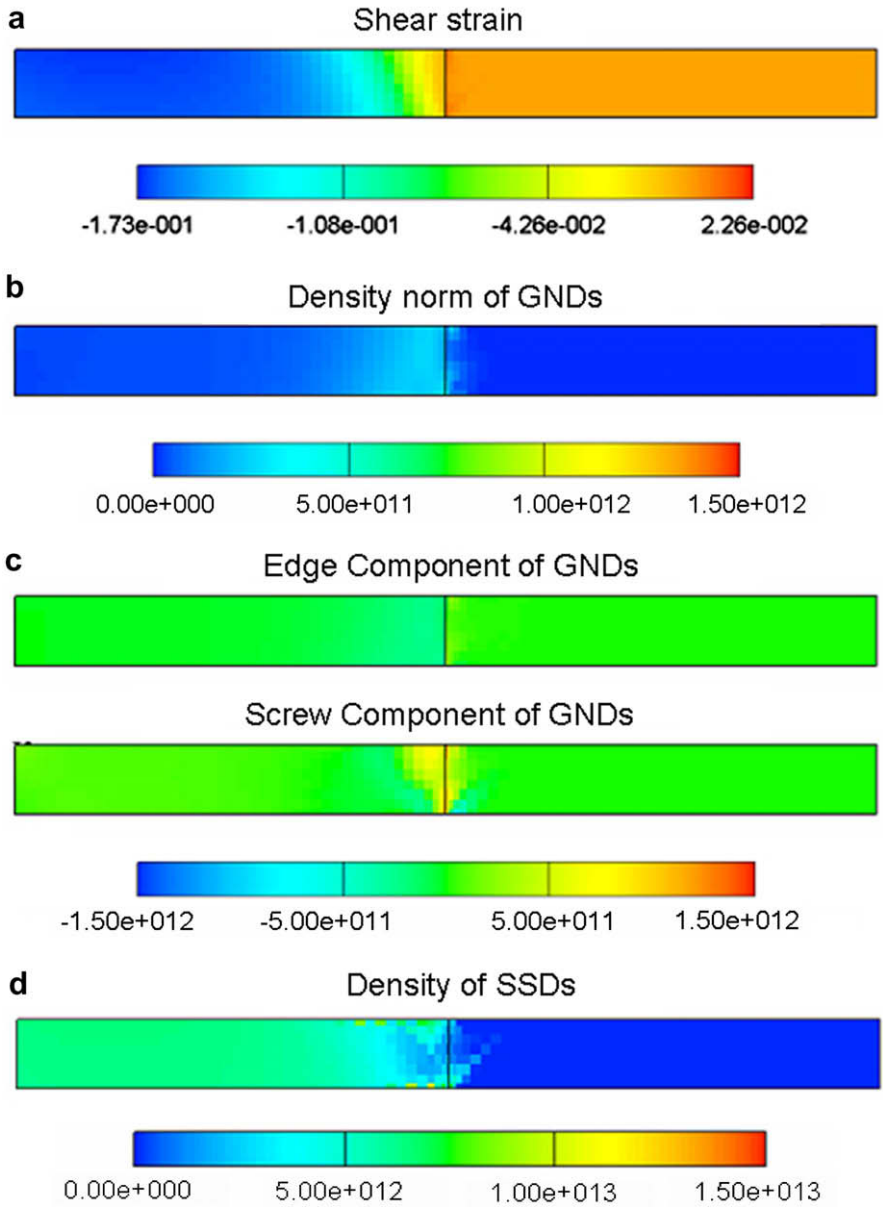

Fig. 15. Distribution of plastic shear strain, density norm of GNDs, edge and screw component of GNDs and SSDs on the $(\bar{1}11)[101]$ slip system when the nominal strain is 10% and viewed on the $Z = 0.3$ mm cross section.

specimen. From these results, following scenario could be developed for the formation of stripe pattern in SSDs. That is, a high density band of GNDs develops due to anisotropic deformation of the bicrystal and GNDs in the band shorten the mean free path of dislocations on $(\bar{1}\,1\,1)[1\,1\,0]$ slip system. Then, a high density of SSDs on $(\bar{1}\,1\,1)[1\,1\,0]$ slip system shorten the mean free path of dislocations on $(1\,1\,1)[1\,0\,\bar{1}]$ in the band and results in the formation of stripe pattern of SSDs on this system. In this way, GN and SS dislocations on more than one slip systems interact in a complicated manner and

sometimes result in a formation of dislocation pattern which could not be expected from simple compatibility requirements at the grain boundary.

It should also be noted that the density of SSDs is approximately ten times larger than that of GNDs even in the high density band of GNDs. It should be noted that the same ratio between GNDs and SSDs density holds for the start of streaking of Laue spots (see Eq. (5)). As is well known, the density of GNDs is scale dependent and the larger the length scale of the material, the smaller the density. Therefore, the interaction of GN and SS dislocations is assumed to be more significant when the specimen size is smaller.

Figs. 15a–d show slip activity and dislocation accumulation on the $(\bar{1}\,1\,1)[1\,0\,1]$ slip system. Shear strain on this slip system is close to zero in the grain B, while in the grain A, the shear strain is about 17% in the grain interior and decreases to zero near the grain boundary. GNDs accumulate near the grain boundary in the grain A (Fig. 15 b) and their character is close to pure screw dislocations (Fig. 15c). Density distribution of SSDs is shown in Fig. 15d. The density of SSDs in the grain A is approximately $7 \times 10^{12}\ \mathrm{m}^{-2}$ in the area far from the grain boundary and it decreases in the vicinity of the boundary. We also notice an accumulation of SSDs in the grain B near the boundary and a part of which makes a stripe pattern, on which we already discussed in some detail.

Fig. 15 shows more or less smooth distribution of shear strain in the grain A, while the slip line pattern obtained in the experiment and shown in Fig. 10 depicts slip bands and other local fluctuations of slip activities. These fluctuations observed in the experiment are assumed to be caused from initial inhomogeneities which are inherent in real materials. Ohashi (1990) showed a mechanism for the formation of slip bands from initial inhomogeneities. Even a small fluctuation of the initial dislocation density or dislocation mean free path was shown to cause the formation of slip bands inside a grain. In this study we are interested in the GNDs behavior in the vicinity of the boundary. For this reason the very remote regions where different inhomogeneities can influence this behavior were not considered.

3.4. Discussion

The plastic response of the material in both A and B grains of the bicrystal can be described by the formation of GN and SS dislocation populations in the material to relax the stress field induced during pulling. In FCC crystals, typical edge dislocation lines are parallel to the directions of $\langle 1\,1\,2 \rangle$ with Burgers vectors being parallel to the directions $\langle 1\,1\,0 \rangle$ and corresponding glide planes $\{1\,1\,1\}$ (see Table 2). Formation of the narrow slip bands separating regions with low GN density can be understood from the view point of mesoscopic self-organized structures. Such self-organization decreases the free energy of the system. Formation of similar narrow microbands with localized lattice rotations was observed during rolling and torsion of polycrystalline Ni (Hansen and Hughes, 1995; Bay et al., 1992). Several models for grain subdivision during plastic deformation were proposed (Jakobsen et al., 2006; Seefeldt et al., 2001; Sedlacek et al., 2002; Romanov, 2003).

With increasing strain due to collective behavior in the interacting dislocation ensemble, rotational plastic modes appear. Rotations are localized in narrow microbands separating the grain into strongly disoriented regions (Hansen, 2005). This process can be schematically described as following: (1) randomly distributed dislocations, (2) cell-wall structure; (3) microbands with IDBs and GNBs. As deformation increases the cell boundaries become narrower and result in the formation of IDBs and GNBs. At the micro and mesoscales the spontaneous reconstruction of dislocation substructure is a typical sign of the nonlinear behavior of the deformed material. At low-strain deformation without strain gradients the SS dislocation density is an important parameter of the deformed crystal. With increasing strain SS randomly distributed dislocations reconstruct with a formation of the cell-wall structure (Mughrabi, 1983; Mughrabi and Obst, 2005). Under strain gradients, the density of GNDs and GNBs controls formation of microbands with localized rotational modes. Formation of each type of dislocation substructure depends not only on the external strain fields but also on the interaction between already existing dislocations (and defects). With the increase of dislocation density the average distance between them decreases, and dislocation/dislocation interaction increases, resulting in the collective phenomena and self-organization in the dislocation ensemble (Seefeldt et al., 2001; Romanov, 2003).

4. Summary

The dislocation arrangement for patterning at several structural levels involved during *in situ* uniaxial pulling of a Ni bicrystal at 0%, 12% and 16% macroscopic plastic strain was investigated. Two bicrystals were employed: one is real and used in the experiment and the other one in a model used for numerical analysis. The orientation relationship of grains components for the two bicrystals are the same. The parallel theoretical background of GNDs characterization with special experimental polychromatic microdiffraction and with the crystal plasticity analysis and evaluation of GNDs is also described. Links are discussed between experimental and simulation methods. Both techniques were utilized to measure the GND densities distribution in the vicinity of the grain boundary.

Results of the numerical analysis show that the model bicrystal deforms, under tensile load, mainly by the activity of two slip systems, which are $(1\,1\,1)[1\,0\,\bar{1}]$ and $(\bar{1}\,1\,1)[1\,0\,1]$. The slip system $(1\,1\,1)[1\,0\,\bar{1}]$ is active only in one grain and the other slip system, $(\bar{1}\,1\,1)[1\,0\,1]$ is active only in the other grain. Morphologies for the density distributions of GNDs on the two slip systems are distinctly different.

On the slip system $(1\,1\,1)[1\,0\,\bar{1}]$, GNDs make up a high density band which emerges from the intersection of the grain boundary and the specimen surface and develops into the interior of a grain (Fig. 14). On the other slip system, the GNDs density is highest at the grain boundary and decreases gradually with distance from the boundary (Fig. 15). The above mentioned features of the density distribution of GNDs are in good agreement with the experimental results (Fig. 6), in that GND density is high at the grain boundary and decrease with distance from the boundary in the Grain A, while the GND density in the Grain B is very low at the grain boundary and show a high value inside a narrow band in the grain interior. Numerical results also show that SSDs on both slip systems make up high density bands.

The formation of geometrically necessary (GN) and statistically stored (SS) dislocation arrangements together with lattice rotations were observed during *in situ* uniaxial pulling of a natural Ni bicrystal. The density of GN dislocations oscillates locally resulting in the formation of narrow slip bands with high GN dislocations density in them separated with regions having low GN dislocation density. Local lattice rotations and GN dislocation density depends on the distance from the boundary, depth of the location under the surface and on the orientation of the grain relative to the tensile axis. In the vicinity of the boundary, oscillating dislocation structure was observed in the A grain, while lattice rotations dominated in the B grain. In contrast large dilatational strain of the lattice was observed at a large distance form the boundary in the grain B while in the grain A strain decreased relatively quickly. Crystal plasticity analysis together with finite element simulation find a similar dependence of the plastic response of both grains depending on their orientation and initial structural conditions.

Acknowledgements

Experimental research is supported by the Division of Materials Science and Engineering, Office of Basic Energy Science and the ORNL SHARE user facility, US Department of Energy. Synchrotron measurements on Unicat beamline 34-ID at the Advanced Photon Source (APS), were also supported by the US Department of Energy, Office of Science. One of the authors (T.O.) acknowledges that finite element work was performed under financial support from the Ministry of education, culture, sports, science and technology under Grant No. 18062001. The author also acknowledges Dr. Ryouji Kondou for his effort in numerical analysis.

References

Arsenlis, A., Parks, D.M., 1999. Crystallographic aspects of geometrically-necessary and statistically-stored dislocation density. Acta Materialia 47 (5), 1597–1611.

Arsenlis, A., Parks, D.M., Becker, R., Bulatov, V.V., 2004. On the evolution of crystallographic dislocation density in non-homogeneously deforming crystals. Journal of the Mechanics and Physics of Solids 52, 1213–1246.

Barabash, R.I., Ice, G.E., 2005. Microdiffraction analysis of hierarchical dislocation organization. In: Encyclopedia of Materials: Science and Technology Updates. Elsevier, Oxford, pp. 1–18.

Barabash, R., Pantleon, W., 2004. Characterization of dislocation boundary evolution with monochromatic X-ray diffraction. In: Proceedings of the 25th Risø International symposium on Materials Science: Evolution of Deformation icrostructures in 3D, pp. 233–238.

Barabash, R.I., Ice, G.E., Larson, B.C., Pharr, G.M., Chung, J.-S., Yang, W., 2001. White microbeam diffraction from distorted crystals. Applied Physics Letters 79, 749–751.
Bardella, L., 2007. Some remarks on the strain gradient crystal plasticity modeling, with particular reference to the material length scale involved. International Journal of Plasticity 23, 296–322.
Bay, B., Hansen, N., Hughes, D.A., Kuhlmann-Wilsdorf, D., 1992. Evolution of F.C.C. deformation structures in polyslip. Acta Metallurgica and Materialia 40, 205–219.
Beyerlein, I.J., Tome, C.N., 2008. A dislocation-based constitutive law for pur Zr including temperature effects. International Journal of Plasticity 24, 867–895.
Bonifaz, E.A., Richards, N.L., 2008. The plastic deformation of non-homogeneous polycrystals. International Journal of Plasticity 24, 289–301.
Chen, Q.Z., Jones, C.N., Knowles, D.M., 2004. The grain boundary microstructures of the base and modified RR 2072 bicrystal superalloys and their effects on the creep properties. Materials Science and Engineering A 385, 402–418.
Feng, Lu, Zhang, Guang, Zhang, Ke-shi, 2003. Materials Science and Engineering A 361, 83.
Gao, H., Huang, Y., Nix, W., Hutchinson, J., 1999. Mechanism-based strain gradient plasticity – I. Theory. Journal of the Mechanics and Physics of Solids 47, 1239–1263.
Gurtin, M.E., 2008. A finite-deformation, gradient theory of single-crystal plasticity with free energy dependent on densities of geometrically necessary dislocations. International Journal of Plasticity 24, 702–725.
Han, C.-S., Ma, A., Roters, F., Raabe, D., 2007. A finite element approach with patch projection for strain gradient plasticity formulations. International Journal of Plasticity 23, 690–710.
Hansen, N., 2005. Boundary strengthening over five length scales. Advanced Engineering Materials 7, 815–821.
Hansen, N., Hughes, D.A., 1995. Analysis of large dislocation populations in deformed metals. Physica Status Solidi (b) 149, 155–172.
Hill, R., 1966. Generalized constitutive relations for incremental deformation. Journal of the Mechanics and Physics of Solids 14, 95–102.
Hirth, J.P., Pond, R.C., Lothe, J., 2006. Disconnections in tilt walls. Acta Materialia 54, 4237–4245.
Huang, Y., Gao, H., Nix, W., Hutchinson, J., 2000. Mechanism-based strain gradient plasticity-II. Journal of the Mechanics and Physics of Solids 48, 99–128.
Huang, E.-W., Barabash, R.I., Wang, Y., Clausen, B., Li, L., Liaw, P.K., Ice, G.E., Ren, Y., Choo, H., Pike, L.M., Klarstrom, D.L., 2008. Plastic behavior of a nickel-based alloy under monotonic-tension and low-cycle-fatigue loading. International Journal of Plasticity 24, 1440–1456.
Ice, G.E., Barabash, R.I., 2007. White beam microdiffraction and dislocations gradients. In: Dislocations in Solids, vol.13, pp. 500–601 (Chapter 79).
Ice, G.E., Larson, B.C., 2002. 3D X-ray crystal microscope. Advanced Engineering Materials 2 (10), 643.
Jakobsen, B., Lienert, U., Almer, J., Shastri, S.D., Sorensen, H.O., Gundlach, C., Pantleon, W., 2006. Formation and subdivision of deformation structures during plastic deformation. Science 312, 889–892.
Kocks, U.F., Mecking, H., 2003. Physics and phenomenology of strain hardening: the FCC case. Progress in Materials Science 48, 171–273.
Kuhlmann-Wilsdorf, D., 1989. Theory of plastic deformation: properties of low energy dislocation structures. Materials Science and Engineering A113, 1.
Kuhlmann-Wilsdorf, D., Hansen, N., 1991. Geometrically necessary, incidental and subgrain boundaries. Scripta Metallurgica and Materialia 25, 1557–1562.
Larson, B.C., Yang, W., Ice, G.E., Budai, J.D., Tischler, J.Z., 2002. Three-dimensional X-ray structural microscopy with submicron resolution. Nature 415, 887.
Larson, B.C., El-Azab, A., Yang, W., Tischler, J.Z., Liu, W., Ice, G.E., 2007. Experimental characterization of the mesoscale dislocation density tensor. Philosophical Magazine 87 (8-9), 1327–1347.
Levine, L.E., Larson, B.C., Yang, W., Kassner, M.E., Tischler, J.Z., Delos-Reyes, M.A., Fields, R.J., Liu, W., 2006. X-ray microdiffraction measurements of individual dislocation cell elastic strains in deformed single-crystal copper. Nature Materials 5, 619–622.
Lu, F., Guang, Z., Ke-shi, Z., 2003. Grain boundary effects on the inelastic deformation behavior of bicrystals. Materials Science and Engineering A 361, 83–92.
Miura, H., Ozama, M., Mogava, R., Sakai, T., 2003. Strain rate effect on dynamic recrystallization at grain boundary in Cu alloy bicrystal. Scripta Materialia 48, 1501–1505.
Miura, H., Sakai, T., Mogawa, R., Gottstein, G., 2004. Nucleation of dynamic recrystallization at grain boundaries in copper bicrystals. Scripta Materialia 51, 671–675.
Monzen, R., Watanabe, C., Mino, D., Saida, S., 2005. Initiation and growth of the discontinuous precipitation reaction at [011] symmetric tilt boundaries in Cu–Be alloy bicrystals. Acta Materialia 53, 1253–1261.
Mughrabi, H., 1983. Dislocation wall and cell structures and long-range internal stresses in deformed metal crystals. Acta Metallurgica 31 (9), 1367–1379.
Mughrabi, H., Obst, B., 2005. Misorientations and geometrically necessary dislocations in deformed copper crystals: a microstructural analysis of X-ray rocking curves. Zeitschrift fur Metallkunde 96 (7), 586–695.
Nabarro, F.R.N., 2001. Sequences of dislocation patterns. Materials Science and Engineering A317, 12–16.
Nye, J.F., 1953. Some geometrical relations in dislocated crystals. Acta Metallurgica 1, 153–162.
Ohashi, T., 1987. Computer simulation of non-uniform multiple slip in face centered cubic bicrystals. Transactions of Japan Institute of Metals 28, 906–915.
Ohashi, T., 1990. Numerical analyses of deformation band evolution in face-centered cubic single crystals under tensile deformation. Material Transactions, Japan Institute of Metals 31, 456–462.
Ohashi, T., 1994. Numerical modeling of plastic multislip in metal crystals of f.c.c. type. Philosophical Magazine A70, 793–803.
Ohashi, T., 1997. Finite-element analysis of plastic slip and evolution of geometrically necessary dislocations in FCC crystals. Philosophical Magazine Letters 75, 51–57.
Ohashi, T., 1999. Evaluation and visualization of geometrically necessary dislocations in metal microstructures by means of continuum mechanics analysis. Journal of Physics IV France 9. Pr9-279-284.

Ohashi, T., 2005. Crystal plasticity analysis of dislocation emission from micro voids. International Journal of Plasticity 21, 2071–2088.
Ohashi, T., Kawamukai, M., Zbib, H., 2007. A multiscale approach for modeling scale-dependent yield stress in polycrystalline metals. International Journal of Plasticity 23, 897–914.
Romanov, A.E., 2003. Importance of disclinations in severe plastically deformed materials. Advanced Engineering Materials 5, 301–307.
Sauzay, M., 2004. Analytical modeling of intragranular backstresses due to deformation induced dislocation microstructures. International Journal of Plasticity 24, 727–745.
Sedlacek, R., Blum, W., Kratochvil, J., Forest, S., 2002. Subgrain formation during deformation: physical origin and consequences. Metallurgical and Material Transactions A33, 319–327.
Seefeldt, M., Delannay, L., Peeters, B., Kalidindi, S.R., Van Houtte, P., 2001. A disclination-based model for grain subdivision. Material Science Engineering, 192–196.
Spearot, D.E., Jacob, K.I., McDowell, D.L., 2005. Nucleation of dislocations from [0 1 1] bicrystal interfaces in aluminum. Acta Materialia 53, 3579–3589.
Spearot, D.E., Tschopp, M.A., Jacob, K.I., McDowell, D.L., 2007. Tensile strength of $\langle 1\,0\,0 \rangle$ and $\langle 1\,1\,0 \rangle$ tilt bicrystal copper interfaces. Acta Materialia 55, 705–714.
Sun, S., Adams, B.L., King, W.E., 2000. Observation of lattice curvature near the interface of a deformed aluminum bicrystal. Philosophical Magazine A 80 (1), 9–25.
Tschopp, M.A., McDowell, D.L., 2008. Dislocation nucleation in $\Sigma 3$ asymmetric tilt grain boundaries. International Journal of Plasticity 24, 191–217.
Volokh, K.Y., Trapper, P., 2007. A simple theory of strain gradient plasticity on stress-induced anisotropy of defect diffusion. International Journal of Plasticity 23, 2085–2114.
Wang, H., Hwang, K.C., Huang, Y., Wu, P.D., Liu, B., Ravichandran, G., Han, C.-S., Gao, H., 2007. A conventional theory of strain gradient crystal plasticity based on the Taylor dislocation model. International Journal of Plasticity 23, 1540–1554.
Ziegler, A., Campbell, G.H., Kumar, M., Stolken, J.S., 2003. Effects of grain boundary constraint on the Constitutive response of tantalum bicrystals. Materials Research Society Symposium Proceedings 779. W6.4.1.–6.4.6.